

## Progress toward a large-scale ion Talbot-Lau interferometer

Andrea Demetrio,<sup>1,\*</sup> Simon R. Müller,<sup>1</sup> Pierre Lansonneur,<sup>2</sup> and Markus K. Oberthaler<sup>1</sup>

<sup>1</sup>*Kirchhoff-Institut für Physik, Im Neuenheimer Feld 227, 69120 Heidelberg, Germany*

<sup>2</sup>*Institut de Physique Nucléaire de Lyon, CNRS, IN2P3, 69622 Villeurbanne, France*

(Received 27 October 2017; published 4 December 2017)

The Talbot-Lau interferometer is a proven tool to perform measurements in the near-field regime. It has been extensively used for investigating the wave nature of electrons, atoms, and complex organic molecules. However, when designing devices with high geometrical acceptances, which would be desirable when dealing with low-intensity sources of particles, the alignment requirements become much more stringent. Furthermore, if the particles are charged, the influence of external fields becomes quickly non-negligible when increasing the length of the device. This paper focuses on both the geometric and physical constraints of an ion Talbot-Lau interferometer, with emphasis on the scaling of such constraints with the size of the device. Mathematical formulas which set limits on the critical parameters are derived and applied to a test setup for protons.

DOI: [10.1103/PhysRevA.96.063604](https://doi.org/10.1103/PhysRevA.96.063604)

### I. INTRODUCTION

The wave-particle duality is one of the most defining phenomena related to quantum mechanics. Since the experiment performed by Davisson and Germer [1], this constitutive property of matter has been verified several times, for different kind of particles, ranging from electrons [2–4] to organic compounds [5]. A common concept among these experiments is the design and use of a setup which allows the wave function of the particles to self-interfere or be macroscopically diffracted. Among the devices designed for this purpose, the Talbot-Lau near-field interferometer has seen prominent use in the past two decades, having been successfully applied to electrons [6], atoms [7], fullerenes [8], and, in its Kapitza-Dirac variant, even larger organic molecules [9].

A device of this type has been proposed to be used with antiprotons [10], dealing at once with charged particles heavier than the electron and a low-luminosity, highly divergent source. The latter constraint makes an interferometer with a large active area necessary.

However, when scaling up the device to get a higher geometrical acceptance, a precise alignment of all its elements becomes critical. Moreover, when increasing the length of the device, the influence of external forces acting on the particles increases quadratically with its size, setting strict limits on their maximum allowed energy spread, depending on the intensity of the force.

This paper focuses on both the geometrical and the physical constraints of such a device, with emphasis on electric and magnetic interactions which would affect the design of an ion Talbot-Lau interferometer.

### II. TALBOT-LAU INTERFEROMETER

In its most common variant, the Talbot-Lau interferometer is composed of two material gratings with periodicity  $d$  and open fraction  $\eta$ . The two gratings are spaced by a distance  $L$ . A diffusive beam of particles with de Broglie wavelength  $\lambda_{\text{dB}}$  impinging on the first grating generates an interference pattern,

as shown in Fig. 1. The pattern appears as a density modulation with periodicity  $d$  and corresponding position  $\phi = 2\pi y/d$  when observed on a plane placed at the same distance  $L$  from the second grating.

The device described so far can act in the classical regime, in the near-field wave regime, or in the far-field wave regime, depending on its geometrical parameters. The typical length scale which is considered to distinguish the three regimes is called the Talbot length and is defined as

$$L_T = \frac{d^2}{\lambda_{\text{dB}}} = \frac{d^2}{h} \sqrt{2mU}, \quad (1)$$

with  $m$  being the mass of the particle,  $U$  the kinetic energy, and  $h$  the Planck constant. If  $L \gg L_T$ , the device operates in the far-field regime as a Mach-Zehnder interferometer [11]. In this configuration, the contrast of the pattern, defined as

$$C = \frac{I_{\text{max}} - I_{\text{min}}}{I_{\text{max}} + I_{\text{min}}}, \quad (2)$$

where  $I_{\text{max}}$  and  $I_{\text{min}}$  are the maximum and the minimum intensity, respectively, reveals no dependence on the de Broglie wavelength of the particles (achromatic setup) [12]. If  $L \approx L_T$ , the device operates in the near-field regime and the contrast shows a dependence on both the energy of the particles and the open fraction  $\eta$  of the gratings, as shown in Fig. 2. This is what is referred to as the Talbot-Lau interferometer. In the limit of  $L \ll L_T$ , the pattern is generated by the classical trajectories of the particles. This is again an achromatic setup, with the contrast of this pattern depending only on the open fraction  $\eta$ . A device which operates in these conditions is commonly referred to as the moiré deflectometer [13–15]. For specific configurations satisfying  $L = nL_T$ , with  $n \in \mathbb{Z}^+$ , the Talbot-Lau interference pattern is indistinguishable from the corresponding classical pattern [16,17]. The ideal configuration to reveal the wave behavior of the test particles is therefore not at this resonance condition.

In a typical experiment, the length of the device is fixed, while the energy of the particles is tuned. Thus one expects that for certain energies  $U_n$  the condition  $L = nL_T$  is fulfilled.

\*Corresponding author: talbotsystematics@matterwave.de

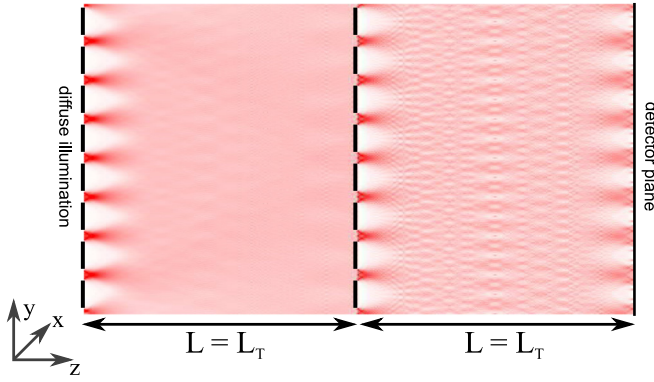


FIG. 1. Diffuse illumination (light, particles) impinging on a Talbot-Lau interferometer generates the so-called Talbot carpet. The first grating generates the spatial coherence, allowing the second grating to create the pattern. A third grating can be used to read the pattern.

These energies are directly derived from Eq. (1):

$$U_n = \frac{U_{\text{Talbot}}}{n^2} = \frac{h^2 L^2}{2md^4} \frac{1}{n^2}, \quad n \in \mathbb{Z}^+. \quad (3)$$

In order to reveal quantum interference, these specific rephasing distances (energies) are not useful, but a modulation of the contrast as a function of the energy is a clear indicator of the wave behavior of the test particles.

In an experimental realization of the device, the periodic pattern can be read out with the use of a position-sensitive detector. If the periodicity of the pattern is smaller than the resolution of the detector, the use of a third grating, identical to the first two, is required to extract the information: When the additional grating is tilted around the beam axis, beatings with periodicity inversely proportional to the rotation angle appear,

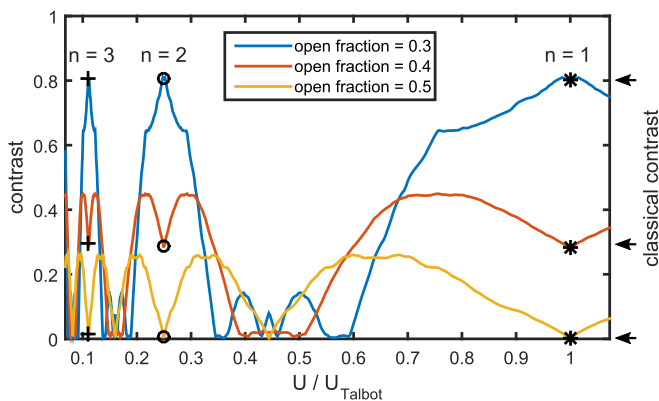


FIG. 2. Contrast of the pattern as a function of the energy of a proton beam. This plot is valid for a device composed of three gratings, the third one being scanned [13] or tilted [15] to read out the pattern. The shape of the contrast profile is strongly affected by the open fraction  $\eta$  of the gratings. The black markers highlight  $U = U_n$  for  $n = 1, 2, 3$  where the Talbot-Lau signal is indistinguishable from the classic moiré signal [see Eq. (3)]. The plot has been calculated following the approach by Hornberger *et al.* [16], based on calculating the intensity pattern using the Wigner representation [18]. The plots are arranged from top to bottom, according to the legend.

making the interference pattern observable on a large scale [15], thus allowing for the use of a detector with a significantly reduced constraint on the spacial resolution. As an alternative, the third grating can be used to scan the original pattern, by translating it in the direction perpendicular to the slits and recording the transmitted particle flux for every position [9,13]. The device considered in the following discussion employs a scanned third grating.

It is worth mentioning that the Kapitza-Dirac variant of the Talbot-Lau interferometer, which replaces the second grating with a standing wave [9,19], does not provide a significant advantage when working with ions. The interaction rate scales like  $m^{-1/2}$ , requiring a significantly higher laser power than for electrons (which is of the order of  $\text{GW cm}^{-2}$ ) [20,21] to achieve similar results, and the interaction area of the phase grating cannot be scaled to larger sizes without defocusing the laser and thus losing significant intensity. Furthermore, the use of a pulsed laser with a continuous source of particles implies that the duty cycle of the laser ( $\approx 10^{-7}$ ) directly translates into a flux reduction within the interferometer.

### III. CONTRAST REDUCTION DUE TO SYSTEMATIC EFFECTS

While the ideal contrast of the interference pattern is only dependent on the energy of the particles, once the device geometry is fixed, in any experimental realization it is strongly dependent on the alignment of the device and on the influence of external forces, such as gravity or electric interactions. In this section, we discuss three families of systematic effects which concur in degrading the quality of the signal: misalignment of the gratings, energy spread of the particle source, and external forces acting on the particles. In the latter, emphasis is put on the Lorentz force interaction, which becomes prominent when dealing with charged particles.

For the following discussion, we use specific experimental parameters which are currently available. The production of nanometric gratings with thin silicon nitrate membranes, like the ones described in Ref. [22], limits the energy of the charged particles due to the limited stopping power of the material. Thus we consider a proton source with tunable energy in the keV regime, of the type covered in Ref. [23]. In this configuration,  $\lambda_{\text{dB}} \approx 1$  pm. The geometrical parameters of the device are  $d = 256$  nm,  $L = 171.7$  mm, and  $\eta = 0.4$ , thus yielding  $U_{\text{Talbot}} = 5.64$  keV. The classical rephasing is thus expected also for  $U_2 = 1.41$  keV and  $U_3 = 627$  eV.

#### A. Geometrical constraints

The pattern is extremely sensitive to deviations from the ideal geometry: Differences in the distance between the gratings and the detector plane or small relative tilts of the gratings can consistently affect the quality of the signal. In the following, we consider two specific scenarios: longitudinal asymmetries and rotational misalignment around the beam axis.

##### 1. Longitudinal asymmetry

In the optimal configuration, the device can be operated with a fully divergent source of particles and still produces

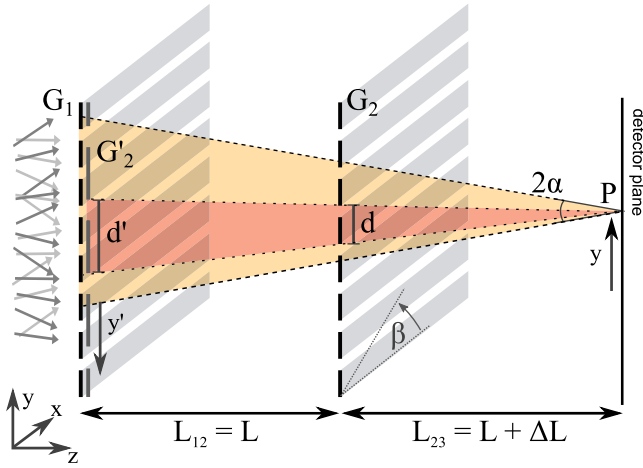


FIG. 3. Schematic showing how the classical pattern is calculated. For every point  $P$  on the detector, the region from where particles can reach the point is calculated by projecting the second grating ( $G_2$ ) on the first one ( $G_1$ ), thus identifying the effective fraction of the particle which contributes to the intensity. The projected grating  $G_2'$  has a magnified periodicity  $d'$ , as in Eq. (5). When considering a source with divergence  $\alpha$ , the region from which a particle can reach the detector is limited by a cone with opening angle  $\alpha$  equal to the divergence of the source (bright region). The tilt angle  $\beta$  is considered when extending the approach to three dimensions. The analytic treatment is explained in detail in the text.

a pattern with the expected maximal contrast. In any experimental scenario, the divergence of the source puts constraints on its geometrical characteristics: An asymmetry  $\Delta L$  between the distance from the first to the second grating  $L_{12}$  and the distance from the second to the third grating  $L_{23}$  strongly affects the contrast of the pattern. The effects of this asymmetry can be calculated analytically in the simple case of a moiré deflectometer, whose signal is equivalent to the Talbot-Lau interferometer whenever the length of the device matches a multiple of  $L_T$ .

The process is schematized in Fig. 3. Consider a point  $P$  on the detector plane. We calculate the intensity of the signal which illuminates this point by considering the allowed geometrical trajectories. All the particles which reach  $P$  have to pass through both gratings, indicated as  $G_1$  and  $G_2$ , respectively, therefore limiting their original position to a specific region of space. In the case of  $G_2$ , this region can be interpreted as its shadow image  $G_2'$ , obtained using  $P$  as a focal point. Suppose we have a source with divergence  $\alpha$ ,  $L_{12} = L$ ,  $L_{23} = L + \Delta L$ , grating periodicity  $d$ , and open fraction  $\eta$ . The grating function  $G$  as a function of the position  $y$  is defined as

$$G(y; d, \eta) = \begin{cases} 1 & \text{for } \text{mod}(y, d) < \eta d \\ 0 & \text{otherwise.} \end{cases} \quad (4)$$

As a result, the projected image  $G_2'$  can be described as a grating with the same open fraction  $\eta$  and a magnified periodicity  $d'$ , given by

$$d' = d \frac{L_{12} + L_{23}}{L_{23}} = d \frac{2L + \Delta L}{L + \Delta L}. \quad (5)$$

To calculate the intensity at  $P$ , the grating  $G_2$  can therefore be replaced by its projection  $G_2'$  on the plane of the first grating [24]. As shown in Fig. 3, while moving the projection point by a distance  $y$  on the screen,  $G_2'$  moves in the opposite direction by a position  $y'$  given by

$$y' = \frac{L}{L + \Delta L} y. \quad (6)$$

In the following,  $G_1 = G(y; d, \eta)$ ,  $G_2' = G(y'; d', \eta)$ . If we consider a completely divergent particle source, the intensity  $I_{\text{det}}$  at any position  $y$  on the detector plane is given by

$$I_{\text{det}}(y) \propto \int_{-\infty}^{+\infty} G(\xi; d, \eta) G(\xi + y'; d', \eta) d\xi. \quad (7)$$

In this scenario,  $\Delta L \neq 0$  causes the contrast of the fringes generated by the first two gratings to vanish completely, as the rephasing is only seen at integer multiples of  $L_{12}$ . As mentioned in Sec. II, a third grating placed on the detector plane can be used to read out the pattern. In this case, the intensity  $I$  after the additional grating  $G_3 = G(y; d, \eta)$  is given by

$$I(y_g) \propto \int_{-\infty}^{+\infty} I_{\text{det}}(\xi) G(\xi - y_g; d, \eta) d\xi, \quad (8)$$

where  $y_g$  is the position of the third grating. If we put constraints on the divergence of the beam, the area from where particles can hit the detector is limited to a region of space  $\xi \in [y - y_{\text{lim}}, y + y_{\text{lim}}]$ , where  $y_{\text{lim}} = (2L + \Delta L) \tan(\alpha)$  is the geometrical limit imposed by the divergence angle  $\alpha$  and  $y$  is the coordinate of the detector point at which the pattern is calculated (see Fig. 3). With these assumptions, Eq. (7) becomes

$$I_{\text{det}}^\alpha(y) \propto \int_{y - y_{\text{lim}}}^{y + y_{\text{lim}}} G(\xi; d, \eta) G(\xi + y'; d', \eta) d\xi. \quad (9)$$

The intensity  $I^\alpha(y_g)$  after the third grating is then calculated as in Eq. (8):

$$I^\alpha(y_g) \propto \int_{-\infty}^{+\infty} I_{\text{det}}^\alpha(\xi) G(\xi - y_g; d, \eta) d\xi. \quad (10)$$

The contrast of the pattern as a function of  $\Delta L$  shows a main peak at  $\Delta L = 0$ , together with smaller secondary peaks of decreasing intensity. An example of this behavior is shown in Fig. 4. For a completely divergent source ( $\alpha \rightarrow \pi/2$ ), Eq. (10) converges to Eq. (8), thus yielding the same result. For a given angle  $0 \leq \alpha < \pi/2$ , the position of the first minimum can be calculated via geometric considerations [25]:

$$\Delta L_{\text{min}} = \frac{d}{2} \tan\left(\frac{\pi}{2} - \alpha\right). \quad (11)$$

In the limit of a small divergence angle ( $\alpha \ll 1$ ), this formula is consistent with the one outlined in Ref. [26,27]. As the equation shows,  $\Delta L_{\text{min}}$  is independent of  $L$ : Once the diffusion angle and the periodicity of the gratings are fixed, the other geometrical parameters do not play any role in determining how the contrast decays. A consequence of this systematic effect is that, depending on the divergence of the source, there is a maximum acceptable displacement after which the contrast drops sharply, which can be defined as the position of the first minimum expressed by Eq. (11). Notice that for  $\alpha \approx \pi/2$ ,

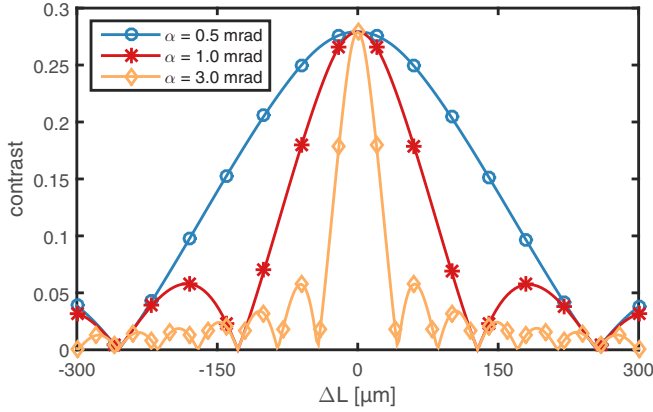


FIG. 4. Contrast of the classical moiré pattern as a function of  $\Delta L = L_{23} - L_{12}$ . When the distance  $\Delta L \neq 0$ , the contrast of the periodic pattern decays as a function of  $\Delta L$  and the divergence angle  $\alpha$ . For  $\Delta L = d/2 \tan(\pi/2 - \alpha)$ , the contrast is equal to zero. The position of the zeros is completely determined by those two parameters and is not affected by the magnitude of  $L_{12}$ .

$\Delta L_{\min}$  tends to zero (i.e., the contrast profile tends to a  $\delta$  centered in  $\Delta L = 0$ ), while for  $\alpha = 0$  (i.e., no divergence),  $\Delta L_{\min}$  goes to infinity, which means that the contrast is not fading away with distance.

As previously pointed out, this mathematical formulation is valid in the classical scenario, but can be verified also in the wave regime by means of numerical simulations. The simulations performed show that for a range of lengths around  $L = L_T$ , the position of the first contrast minimum is consistent with the classical scenario. An example of this behavior is shown in Fig. 5. The classical result can therefore still be considered as the maximum displacement allowed while working in this region.

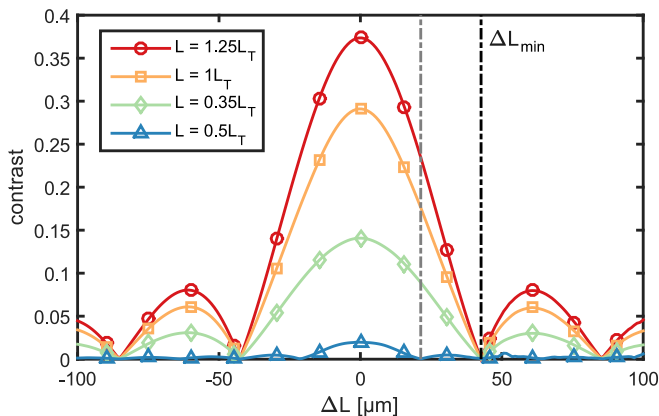


FIG. 5. As in the classical case, the functional dependence of the contrast on the diffusion angle in the Talbot-Lau regime shows periodic minima, the first of which is described by Eq. (11) (black vertical line). Notice that the peak contrast changes with the length. Around  $L = n + \frac{1}{2}L_T$ , the periodicity of the pattern doubles, moving the first minimum at half its classical position (gray vertical line). The profile shown is calculated for a divergence angle  $\alpha = 3$  mrad.

## 2. Rotational misalignment

In the ideal case, the two gratings which generate the pattern have the same rotation angle with respect to the beam axis. When this condition is not fulfilled, the contrast of the pattern depends on the divergence of the source. In order to estimate this effect, we extend the same approach discussed in Sec. III A 1 to two dimensions, allowing for one or both gratings to be tilted around the beam axis.

As an intuitive explanation, consider two gratings: the first one placed in the  $xy$  plane with slits parallel to the  $y$  axis and the second rotated by an angle  $\beta$  around the  $z$  axis (shown in Fig. 3). Consider also a divergence angle  $\alpha$  in the  $yz$  plane, while no diffusion is present in the  $\hat{x}$  direction. If we take a set of planes parallel to the  $yz$  plane and we use it to slice through the pattern for different values of  $x$ , we get a collection of one-dimensional representations equivalent to the one discussed in Sec. III A 1, with the difference that in every plane the pattern of the second grating will show an offset  $\phi_y = x \tan(\beta)$  and a modified periodicity  $d_\beta = d/\cos(\beta)$ . When a divergence in the  $\hat{x}$  direction is considered, all the slices which are between a cone with angular opening  $\alpha$  and the point on the screen at which the pattern is calculated have to be summed up. The combination of these two factors is what smears out the contrast of the generated pattern on the detection plane. By introducing the two-dimensional grating function  $G_{2D}(x, y; \beta, d, \eta)$ , defined as

$$G_{2D}(x, y; \beta, d, \eta) = \begin{cases} 1 & \text{for } \text{mod}(y - x \tan(\beta), d/\cos(\beta)) < \eta d/\cos(\beta) \\ 0 & \text{otherwise,} \end{cases} \quad (12)$$

Eq. (9) can be extended as

$$I_{\text{det}}^{2D}(x, y) \propto \int_{y-r_{\text{lim}}}^{y+r_{\text{lim}}} \int_{x-\sqrt{r_{\text{lim}}^2-(\xi-y)^2}}^{x+\sqrt{r_{\text{lim}}^2-(\xi-y)^2}} G_{2D}(u, \xi; 0, d, \eta) \times G_{2D}(u + x', \xi + y'; \beta, d', \eta) du d\xi. \quad (13)$$

This formula considers a conical projection from the point  $P = (x, y)$  and therefore a circular overlapping area of radius  $r_{\text{lim}} = (2L + \Delta L) \tan(\alpha)$  on the plane of the first grating. Here  $d'$  is expressed by Eq. (5), while  $x'$  and  $y'$  are both defined by using Eq. (6) on  $x$  and  $y$ , respectively. Notice that, as an effect of the angular difference, the resulting fringe pattern is tilted by an angle  $\beta_{\text{pattern}} = 2\beta$ . To retrieve the profile after a third grating, Eq. (10) is also expanded in two dimensions in a similar fashion.

The intensity profile can be evaluated numerically. The calculations show that even when the asymmetry factor is taken out ( $\Delta L = 0$ ), the contrast of the recorded pattern decreases as the angle between the two gratings increases. This phenomenon is independent of the presence of a third grating, since the pattern becomes uniform for a geometrical overlap of the trajectories due to the relative rotation of the first two gratings. By geometric considerations, we derive the following formula for the angular difference  $\beta_{\text{crit}}$  which causes the contrast to drop to zero:

$$\tan \beta_{\text{crit}} = k \frac{d}{2L} \tan\left(\frac{\pi}{2} - \alpha\right), \quad (14)$$

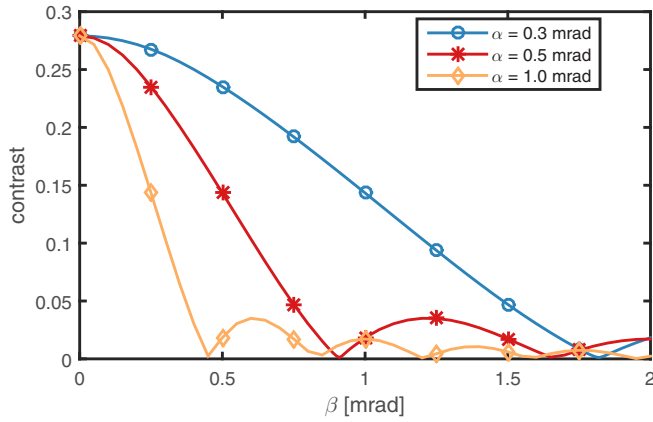


FIG. 6. Depending on the divergence angle  $\alpha$ , an angular difference  $\beta$  between the second and the first grating causes the signal to vanish. The position of the contrast minimum is linearly dependent on  $d$  and inversely proportional to  $L$ . The function which describes this position is similar to the one found for the one-dimensional case [compare Eqs. (11) and (14)].

where  $k$  is a constant factor, to be determined via numerical calculations. Profiles for a different divergence angle  $\alpha$  are shown in Fig. 6. Notice that the formula shows the same functional dependence as in the one-dimensional case [see Eq. (11) as a comparison].

In the representative geometrical configuration, for a divergence  $\alpha = 1$  mrad, the visibility minimum appears for  $\beta = (0.46 \pm 0.01)$  mrad. Repeating the simulations for different geometrical configurations yields  $k = 0.61 \pm 0.01$  as the value for the constant.

It is worth mentioning that, when using a third grating to scan the pattern, the retrieved flux modulation is affected by a rotation of the third grating, due to the moiré effect. Therefore, the rotation angle  $\beta_3$  of the third grating with respect to the pattern has to fulfill the condition

$$\sin\left(\frac{\beta_3}{2}\right) \ll \frac{d}{2\sqrt{A}}, \quad (15)$$

where  $A$  is the area over which the flux is integrated.

### B. Energy spread of the particle beam

Experimental ion sources are not perfectly monochromatic: The particle beam produced always has a nonzero energy spread. As shown in Fig. 2, particles with different energies generate patterns with different contrast: Having an energy distribution means that different patterns get summed up, leading to modifications to the recorded signal. A precise knowledge of the energy distribution is therefore required in order to calculate the expected contrast profile. If the averaging effect is such that the contrast of the pattern becomes lower than or equal to the classical value, the quantum nature of the particle cannot be convincingly proven. Figure 7 shows contrast plots for various energy spreads  $\Delta U/U$ . In the example, the energy distribution is modeled as a normalized Gaussian distribution centered on each energy. The energy spread is thus defined as the full width half maximum (FWHM) of each distribution. As can be seen in Fig. 7, the effect is not

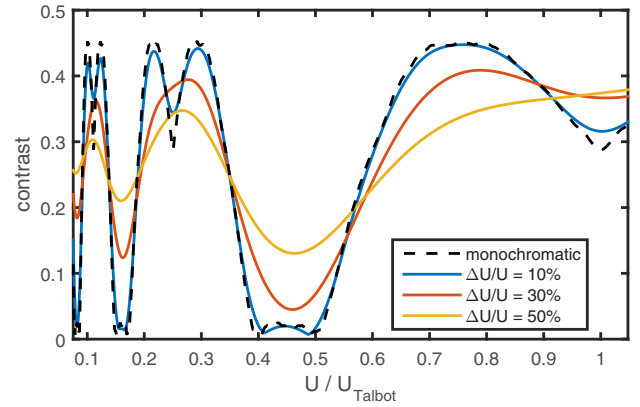


FIG. 7. Contrast of the pattern as a function of the energy of the particle beam for different values of the energy spread. The open fraction considered in this plot is  $\eta = 0.4$ . Each curve is obtained by considering a normal distribution centered on each energy value, with a FWHM equal to the energy spread  $\Delta U$ . For every point on the plot, the ratio  $\Delta U/U$  is fixed to the value shown in the legend. Notice that for an energy spread up to 10%, there is only a negligible difference from the monochromatic case.

dramatic, since even for an energy spread of 30% the contrast modulation is still clearly visible and above the classical expected value for a consistent part of the energy spectrum. Once external forces are taken into consideration, the effect of a nonmonochromatic beam is more accentuated.

### C. External forces

If the particles are affected by an external force  $\vec{F}$  during their crossing of the interferometer, the pattern recorded at the detector position is subject to a phase shift which depends on both the magnitude of the force and the time-of-flight  $\tau$  between the gratings. Assuming a constant acceleration  $a_y$  along the grating periodicity (see the coordinate system in Fig. 1), the phase shift for a monochromatic beam is given by [13]

$$\Delta\phi = \frac{2\pi}{d} a_y \tau^2, \quad (16)$$

with

$$\tau = \frac{L}{v_z} = L\sqrt{\frac{m}{2U}}. \quad (17)$$

Notice that, since the phase shift  $\Delta\phi$  is energy dependent, a force acting on the particles lowers the contrast of the pattern in the presence of an energy spread  $\Delta U$ . A critical force  $\vec{F}_{\text{crit}}$  can therefore be defined as the force leading to a phase shift of  $\pi$  between the fastest and the slowest particles in the distribution. For a given Gaussian energy distribution (mean energy  $U$  and FWHM  $\Delta U$ ) we estimate the critical force assuming  $U_{\text{fast}} = U + \Delta U/2$  and  $U_{\text{slow}} = U - \Delta U/2$ . By considering a uniform constant force, the critical force intensity  $F_{\text{crit}}$  is derived from Eq. (16) as

$$\pi \stackrel{!}{=} \phi_{\text{slow}} - \phi_{\text{fast}} = \pi F_{\text{crit}} \frac{L^2}{d} \left( \frac{\Delta U}{U_{\text{fast}} U_{\text{slow}}} \right), \quad (18)$$

which leads to

$$F_{\text{crit}} = \frac{d}{L^2} \frac{1}{4} \frac{4U^2 - (\Delta U)^2}{\Delta U}, \quad (19)$$

which, in the limit of small energy spread, i.e.,  $(\Delta U)^2 \ll U^2$ , can be further simplified to

$$F_{\text{crit}} \approx \frac{d}{L^2} \frac{U^2}{\Delta U}. \quad (20)$$

Notice that if a generic energy distribution is considered, an integration is instead required to get a precise quantitative result. In the following, two specific examples are considered: a constant Lorentz force and the self-repulsive Coulomb interaction inside a charged particle beam.

### 1. Lorentz force

Charged particles are susceptible to electric and magnetic fields which make the observation of interference more challenging. We therefore assume a Lorentz force for constant uniform fields  $\vec{E}$  and  $\vec{B}$ . Since the interferometer is only sensitive to force acting perpendicular to the grating slits, we are interested in the transverse component of the Lorentz force, which can be written as

$$\vec{F}_y^{\text{Lorentz}} = q[E_y + (v_z B_x - v_x B_z)]\hat{y}, \quad (21)$$

where  $q$  is the charge of the particle.

In the limit of  $v_z B_x \gg v_x B_z$ , which is a reasonable assumption when working with collimated particle beams and assuming the two components of the magnetic fields to have the same order of magnitude, Eq. (21) can be written as

$$\vec{F}_y^{\text{Lorentz}} = q(E_y + v_z B_x)\hat{y}. \quad (22)$$

A definition for the critical electric field  $E_{\text{crit}}$  and magnetic field  $B_{\text{crit}}$  is derived by setting  $\|\vec{B}\|$  and  $\|\vec{E}\|$  to zero, respectively [15]:

$$E_{\text{crit}} = \frac{d}{L^2} \frac{U^2}{q \Delta U} \quad \text{for } \|\vec{B}\| = 0, \quad (23)$$

$$B_{\text{crit}} = \frac{d}{L^2} \sqrt{\frac{m}{2}} \frac{U^{3/2}}{q \Delta U} \quad \text{for } \|\vec{E}\| = 0. \quad (24)$$

In the geometric configuration considered, these fields assume the form

$$\tilde{E}_{\text{crit}} = 8.7 \times 10^{-6} \frac{U}{\delta}, \quad (25)$$

$$\tilde{B}_{\text{crit}} = 6.3 \times 10^{-10} \frac{\sqrt{U}}{\delta}, \quad (26)$$

where  $\delta = \Delta U/U$ ,  $\tilde{E}_{\text{crit}}$  is in units of  $\text{V m}^{-1}$ ,  $U$  is in eV, and  $\tilde{B}_{\text{crit}}$  is in tesla. Notice that, while the critical electric field scales linearly with the energy, the magnetic field scales just with the square root. Therefore, by increasing the energy, the influence of the electric field is reduced faster than that of the magnetic field. If we consider  $U = 2 \text{ keV}$  and  $\delta = 1\%$ , Eqs. (25) and (26) yield  $E_{\text{crit}} = 1.74 \text{ V m}^{-1}$  and  $B_{\text{crit}} = 28.2 \text{ mG}$ , respectively. As a comparison, consider that the fields measured in Ref. [15] in a similar experimental setup are of the order of  $1 \text{ V m}^{-1}$  and  $10 \text{ mG}$ , respectively, already lower than the critical values considered, although no

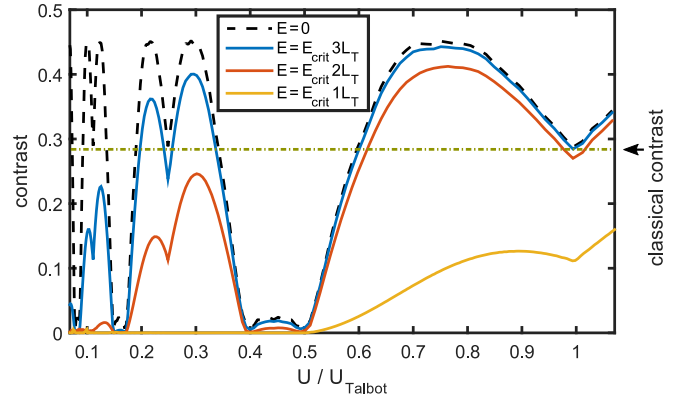


FIG. 8. Effects of external forces, combined with the energy spread of the source, lower the contrast of the pattern. Here we consider  $\Delta U/U = 1\%$ . Each line represents the expected contrast for a given electric field in units of the critical field  $E_{\text{crit}nL_T}$ , defined as in Eq. (27). No magnetic field is considered.

special care has been taken to minimize the fields. Hence, it is reasonable to assume that lower fields are achievable via a suitable electric and magnetic shielding.

Another specific situation which is relevant in this context appears when the distance between the gratings is fixed to an integer multiple of the Talbot length. There the contrast of the pattern is the same as in the classical scenario: This can be a desirable feature to get a reference signal in a known configuration and compare it to the theoretical expectations. Fixing  $L = nL_T$  is equivalent to changing the length of the device for every energy  $U$  used, which is the opposite approach of what was considered above (tuning the energy of the particles in a fixed-length device). With these specifications, Eqs. (23) and (24) can be written as

$$E_{\text{crit}nL_T} = \frac{h^2}{2md^3q} \frac{1}{\delta} \frac{1}{n^2}, \quad (27)$$

$$B_{\text{crit}nL_T} = \frac{h^2}{2\sqrt{2}md^3q} \frac{1}{\delta\sqrt{U}} \frac{1}{n^2}. \quad (28)$$

The expressions underline an interesting fact: If the distance between the gratings is fixed to a multiple of the Talbot length, the critical electric field depends on the relative energy spread  $\delta$  but not directly on the energy. The same does not hold for the critical magnetic field, which instead becomes smaller as the energy increases. An application of Eq. (27) is shown in Fig. 8, where different values of the electric field are applied to a contrast profile with  $\delta = 1\%$ , calculated as the ones shown in Fig. 7.

### 2. Inner beam interactions

When two or more charged particles are moving inside the device, an additional field is generated by their interaction. The particles mutually repel each other, effectively increasing the size of the beam as well as the distance between the center and the edges of the charge distribution. In order to give an upper limit estimation on this effect, consider a beam of particles with mass  $m$  and charge  $q$ . The beam is homogeneous and cylindrical, with initial radius  $r_0$ , axial

velocity  $v_z$ , and uniform charge density  $\rho$ . The beam is assumed to be nonrelativistic ( $\gamma \approx 1$ ), which is a justified approximation in the energy range considered. This has the additional effect of making the contribution of the magnetic fields generated by the moving charge distribution negligible [28]. With these assumptions, the radial electric field  $E_R(r)$  is given by

$$E_R(r) = \begin{cases} \frac{\rho r}{2\epsilon_0} & \text{for } r \leq r_0 \\ \frac{\rho r_0^2}{2\epsilon_0 r} & \text{otherwise.} \end{cases} \quad (29)$$

The field has a maximum for  $r = r_0$ , after which it decreases monotonically. Using this construction, the expanded radius  $r_{\text{beam}}$  at any axial position  $z$  can be calculated by numerically inverting [28]

$$z = \frac{r_0}{\sqrt{2K}} F\left(\frac{r_{\text{beam}}}{r_0}\right) = \frac{r_0}{\sqrt{2K}} \int_1^{r_{\text{beam}}/r_0} \frac{dy}{\sqrt{\ln(y)}}, \quad (30)$$

where the constant  $K$  is given by

$$K = \frac{q\rho r_0^2}{2\pi\epsilon_0 m v_z^2}. \quad (31)$$

It is interesting to note that for  $r_{\text{beam}}/r_0 \ll 1$ ,

$$F\left(\frac{r_{\text{beam}}}{r_0}\right) \simeq 2\sqrt{\frac{r_{\text{beam}} - r_0}{r_0}}, \quad (32)$$

which is equivalent to considering a constant field  $E_R(r_0)$  applied to the particles for the duration of the flight. When  $r_{\text{beam}}/r_0 \ll 1$ , the error introduced by considering this first-order expansion is smaller than 1%. Since we are interested in a beam divergence of the order of the periodicity  $d$  of the grating, until  $d/r_0 \ll 1$ , we can therefore consider a constant radial acceleration  $\vec{a} = qE_R(r_0)/m\hat{r}$ . This has the additional benefit of allowing us to obtain a maximum acceptable value for the particle flux. With this hypothesis, using Eqs. (16) and (29), a particle on the cylinder's surface subjected to  $E_R(r_0)$  experiences a total phase shift

$$\phi = \frac{2\pi y}{d} = \frac{2\pi}{d} a \tau^2 = \frac{2\pi}{d} \frac{q\rho r_0}{2m\epsilon_0} \frac{L^2}{v_z^2}. \quad (33)$$

By expressing  $\rho$  as a function of the particle flux  $\Phi^{\text{in}}$ , we obtain

$$\phi = \frac{2\pi}{d} \Phi^{\text{in}} r_0 \frac{q^2}{2m\epsilon_0} \frac{L^2}{v_z^3} = \frac{2\pi}{d} \Phi^{\text{in}} r_0 \frac{q^2 \sqrt{m}}{4\sqrt{2}\epsilon_0} L^2 U^{-3/2}. \quad (34)$$

In the case that the position shift  $y$  exceeds half the periodicity  $d$  ( $\Delta\phi = \pi$ ), the contrast of the pattern will be consistently reduced. Considering this as the limiting condition, we estimate a critical flux  $\Phi_{\text{crit}}^{\text{in}}$  as

$$\Phi_{\text{crit}}^{\text{in}} = \frac{2\sqrt{2}\epsilon_0}{q^2 \sqrt{m} r_0} \frac{d}{L^2} U^{3/2}. \quad (35)$$

In the geometric configuration analyzed and choosing protons as the test species, with  $U = 2$  keV, it follows that  $\Phi_{\text{crit}}^{\text{in}} = 1.2 \times 10^{15} \text{ m}^{-2} \text{ s}^{-1}$ . By considering, for example,  $r_0 = 1$  mm, we get  $\Phi_{\text{crit}}^{\text{in}} \pi r_0^2 = 3.8 \times 10^9$  Hz. These intensities are well in the range of sources of the type described in Ref. [23], but still far higher than the requirements of a typical experiment (which normally requires  $10^2$ – $10^3$  detected particles on the detector surface to reveal the pattern). Therefore, in the experimental conditions considered, this effect can be consistently neglected.

#### IV. CONCLUSION

In this paper, several systematic effects which degrade the signal of a scalable Talbot-Lau interferometer for charged particles have been analyzed. These effects can be categorized into three distinct families: effects related to the misalignment of the gratings, the energy spread of the source, effects due to the external fields.

A displacement of the detector plane in relation to the distance between the first two gratings causes a consistent reduction of the contrast. The displacement limit which makes the contrast drop to zero is calculated and is found to be independent of the distance between the gratings. Moreover, this displacement is found to be the same both in the particle and in the wave regime. A rotational misalignment between the gratings of the interferometer leads to a reduced contrast as well. Numerical simulations have been used to set limits on this effect in the classical picture. Since both these effects are proportional to the divergence of the beam, they become more restrictive when considering large-area interferometers for low-intensity, noncollimated sources, such as in antimatter experiments.

The energy spread of the source plays a role into averaging the visibility, thus reducing the effective difference in contrast for different energies. However, an energy spread as high as 30% still allows for measuring the wave behavior of the particles.

The presence of external electric or magnetic fields combined with the aforementioned energy spread causes a sharp reduction in contrast, depending on the geometrical characteristics of the device. The limiting force which causes the pattern to vanish is calculated and both the electric and magnetic field intensities are separately obtained. The effects of the inner beam interactions are evaluated and an expression for the maximum flux allowed before said interactions cause a significant drop in contrast is obtained.

#### ACKNOWLEDGMENTS

The authors would like to thank P. Bräunig for advice and useful discussions. The authors are very thankful for the discussions within the AEGIS Collaboration about the feasibility for the realization of a Talbot-Lau interferometer for antiprotons. This work was supported by the Deutsche Forschungsgemeinschaft (Grant No. OB164/10-1).

[1] C. Davisson and L. H. Germer, *Phys. Rev.* **30**, 705 (1927).

[2] C. Jönsson, *Z. Phys.* **161**, 454 (1961).

[3] B. McMorrán, J. D. Perreault, T. Savas, and A. Cronin, *Ultramicroscopy* **106**, 356 (2006).

- [4] R. Bach, D. Pope, S.-H. Liou, and H. Batelaan, *New J. Phys.* **15**, 033018 (2013).
- [5] M. Arndt, O. Nairz, J. Vos-Andreae, C. Keller, G. van der Zouw, and A. Zeilinger, *Nature (London)* **401**, 680 (1999).
- [6] R. Bach, G. Gronniger, and H. Batelaan, *Appl. Phys. Lett.* **103**, 254102 (2013).
- [7] J. F. Clauser and S. Li, *Phys. Rev. A* **49**, R2213 (1994).
- [8] B. Brezger, L. Hackermüller, S. Uttenthaler, J. Petschinka, M. Arndt, and A. Zeilinger, *Phys. Rev. Lett.* **88**, 100404 (2002).
- [9] S. Gerlich, S. Eibenberger, M. Tomandl, S. Nimmrichter, K. Hornberger, P. J. Fagan, J. Tüxen, M. Mayor, and M. Arndt, *Nat. Commun.* **2**, 263 (2011).
- [10] P. Bräunig, J. Storey, and M. K. Oberthaler, AEGIS Collaboration report, 2014 (unpublished).
- [11] G. Gronniger, B. Barwick, and H. Batelaan, *New J. Phys.* **8**, 224 (2006).
- [12] A. Cronin, J. Schmiedmayer, and D. Pritchard, *Rev. Mod. Phys.* **81**, 1051 (2009).
- [13] M. K. Oberthaler, S. Bernet, E. M. Rasel, J. Schmiedmayer, and A. Zeilinger, *Phys. Rev. A* **54**, 3165 (1996).
- [14] S. Aghion *et al.*, *Nat. Commun.* **5**, 4538 (2014).
- [15] P. Lansonneur, P. Bräunig, A. Demetrio, S. R. Müller, P. Nedelec, and M. K. Oberthaler, *Nucl. Instrum. Methods Phys. Res. Sect. A* **862**, 49 (2017).
- [16] K. Hornberger, J. E. Sipe, and M. Arndt, *Phys. Rev. A* **70**, 053608 (2004).
- [17] S. Sala, M. Giammarchi, and S. Olivares, *Phys. Rev. A* **94**, 033625 (2016).
- [18] E. Wigner, *Phys. Rev.* **40**, 749 (1932).
- [19] S. Gerlich, L. Hackermüller, K. Hornberger, A. Stibor, H. Ulbricht, M. Gring, F. Goldfarb, T. Savas, M. Müri, M. Mayor, and M. Arndt, *Nat. Phys.* **3**, 711 (2007).
- [20] D. L. Freimund, K. Afatoon, and H. Batelaan, *Nature (London)* **413**, 142 (2001).
- [21] D. L. Freimund and H. Batelaan, *Phys. Rev. Lett.* **89**, 283602 (2002).
- [22] T. A. Savas, S. N. Shah, M. L. Schattenburg, J. M. Carter, and H. I. Smith, *J. Vac. Sci. Technol. B* **13**, 2732 (1995).
- [23] P. Sortais, T. Lamy, J. Médard, J. Angot, L. Latrasse, and T. Thuillier, *Rev. Sci. Instrum.* **81**, 02B314 (2010).
- [24] F. Bergermann, Diploma thesis, University of Heidelberg, 2012 (unpublished).
- [25] S. R. Müller, internal report, 2017 (unpublished).
- [26] S. Nimmrichter and K. Hornberger, *Phys. Rev. A* **78**, 023612 (2008).
- [27] K. Hornberger, S. Gerlich, H. Ulbricht, L. Hackermüller, S. Nimmrichter, I. V. Goldt, O. Boltalina, and M. Arndt, *New J. Phys.* **11**, 043032 (2009).
- [28] T. Kalvas, in *Proceedings of the CAS-CERN Accelerator School: Ion Sources, Senec, 2012*, edited by R. Bailey (CERN, Geneva, 2013), pp. 537–564.